



Disorientation control on trace element segregation in fluid-affected low-angle boundaries in olivine

Tommaso Tacchetto^{1,2} · Steven M. Reddy^{1,2} · David W. Saxey² · Denis Fougereuse^{1,2} · William D. A. Rickard² · Chris Clark¹

Received: 23 March 2021 / Accepted: 30 June 2021 / Published online: 12 July 2021
© The Author(s), under exclusive licence to Springer-Verlag GmbH Germany, part of Springer Nature 2021

Abstract

The geometry and composition of deformation-related low-angle boundaries in naturally deformed olivine were characterized by electron backscattered diffraction (EBSD) and atom probe tomography (APT). EBSD data show the presence of discrete low-angle tilt boundaries, which formed by subgrain rotation recrystallisation associated with the (100)[001] slip system during fluid-catalysed metamorphism and deformation. APT analyses of these interfaces show the preferential segregation of olivine-derived trace elements (Ca, Al, Ti, P, Mn, Fe, Na and Co) to the low-angle boundaries. Boundaries with $< 2^\circ$ show marked enrichment associated with the presence of multiple, non-parallel dislocation types. However, at larger disorientation angles ($> 2^\circ$), the interfaces become more ordered and linear enrichment of trace elements coincides with the orientation of dislocations inferred from the EBSD data. These boundaries show a systematic increase of trace element concentration with disorientation angle. Olivine-derived trace elements segregated to the low-angle boundaries are interpreted to be captured and travel with dislocations as they migrate to the subgrain boundary interfaces. However, the presence of exotic trace elements Cl and H, also enriched in the low-angle boundaries, likely reflect the contribution of an external fluid source during the fluid-present deformation. The observed compositional segregation of trace elements has significant implications for the deformation and transformation of olivine at mantle depth, the interpretation of geophysical data and the redistribution of elements deep in the Earth. The observation that similar features are widely recognised in manufactured materials, indicates that the segregation of trace elements to mineral interfaces is likely to be widespread.

Keywords Olivine · Deformation microstructures · Grain boundaries · Mineral interfaces · Atom probe tomography · EBSD

Introduction

In monomineralic rocks, grain boundaries mark the change in lattice orientation of adjacent crystals. Grain boundary interfaces are only a few nanometres wide, and represent only a small fraction of the rock volume, yet they play a critical role in controlling physical, rheological and mechanical properties of rocks at a broad range of scales. For example,

diffusion rates along interfaces are orders of magnitude faster than intracrystalline diffusion (Dohmen and Milke 2010) and grain boundary diffusion may facilitate the localized interdiffusion of material within a rock and promote metamorphic reactions (Putnis and John 2010).

Despite the increasing importance of grain boundary characterization in all rocks, the study of grain boundary properties in geological materials has focused primarily on olivine $[(\text{Mg}, \text{Fe})_2\text{SiO}_4]$, because of its importance in the mantle and therefore its role in large-scale geodynamic processes. A significant focus of this research is the characterization of olivine deformation through the quantification of olivine microstructure in naturally and experimentally deformed olivine-rich rocks. Results illustrate that grain boundaries critically affect a number of mantle properties, such as creep strength during diffusion and dislocation creep, element segregation and diffusion rates, as

Communicated by Dante Canil.

✉ Tommaso Tacchetto
tommaso.tacchetto@postgrad.curtin.edu.au

- ¹ School of Earth and Planetary Sciences, Curtin University, Bentley, Perth, WA, Australia
- ² Geoscience Atom Probe Facility, Curtin University, Bentley, Perth, WA, Australia

well as seismic and electrical conductivity properties, all of which have important rheological and geodynamical implications (Wenk 1985; Faul et al. 2004; Rohrer 2011; Hansen et al. 2012; Dillon et al. 2016; Zhao et al. 2019; Yabe and Hiraga 2020). A better understanding of interface properties is key to further developing knowledge of fundamental rock processes.

Detailed microanalytical observations have provided an appreciable visualization of nm-scale structure and composition of grain boundaries in olivine (Kohlstedt 1990; Hiraga et al. 2002, 2003; Marquardt et al. 2015; Marquardt and Faul, 2018). These studies have progressed our understanding of lattice atomic structure (Adjaoud et al. 2012), structural and effective width (Hiraga et al. 2002; Marquardt and Faul 2018; Ricoult and Kohlstedt 1983), and composition (Hiraga et al. 2002, 2003, 2004). Geochemical analyses of high-angle grain boundaries within olivine in deformed mantle rocks have demonstrated the presence of incompatible trace element enrichment, precipitates, and interstitial phases (melt/fluid) at these interfaces (Hiraga et al. 2004). Grain boundaries may therefore be a significant repository of geologically important trace elements (Hiraga et al. 2003, 2004, 2007).

The relationship between adjacent grains and the interface between them can be investigated through the characterization of five geometrical parameters that describe the grain boundary character distribution (GBCD) of a crystalline material (Lloyd et al. 1997). Three of these parameters define the misorientation of the crystal lattice, while the orientation of the boundary plane is constrained by the two additional parameters (Lloyd et al. 1997). Since crystallographic orientations and boundary geometries may change during rock deformation, the GBCD may also vary throughout the deformation cycle. Such relationships have been widely investigated in ceramics and metals (e.g. Lejček 2010), but still represent an emerging field of investigation within naturally occurring geological materials (Marquardt and Faul 2018). The variation in the five GBCD parameters leads to a broad range of possible geometrically distinct grain boundary combinations ($> 60 \times 10^3$ for 10° increments in parameter values, Marquardt et al. 2015), so only a small number of possible boundaries have been studied in detail (Marquardt and Faul 2018). However, the results of these studies have shown that the different types of grain boundaries in olivine-rich rocks may influence the chemical and mechanical properties of the interface region (Marquardt and Faul 2018). Furthermore, it has been shown that segregation of solute ions, precipitates, or interstitial phases, affects the energy and structure of grain boundaries, which in turn may drive the modification of the GBCD, change the interfacial diffusion rate, and affect the rheological behaviour of mantle rocks (Ando et al. 2001; Pang and Wynblatt 2006).

To date, direct observations of mineral grain boundaries have mostly been performed by conventional electron and ion beam-based microscopy techniques (Ando et al. 2001; Hiraga et al. 2002, 2003; Adjaoud et al. 2012; Marquardt et al. 2015, 2018 and references therein) and a clear atomically-resolved visualization of trace element distributions within mineral interfaces has been difficult due to the intrinsic analytical limitations associated with the nanoscale width of these features. Furthermore, the primary focus of these studies has been related to the understanding of structural properties in relation to olivine high-angle phase and grain boundaries whereas the investigation of low-angle boundaries has been generally overlooked. Thus, the relationships between low-angle boundary geometry and composition at the early stages of grain boundary formation, and how this affects the rock properties, are still largely unconstrained.

Atom probe tomography (APT) allows a precise, quantitative, 3D characterization of the sub-nanometre distribution of atoms within grain boundary interfaces (Piazolo et al. 2016; Fougereuse et al. 2019; Montalvo et al. 2019; Cukjati et al. 2019; Reddy et al. 2020). To date, only a few experimental-based investigations have approached the nanoscale characterization of high-angle olivine grain boundaries by atom probe tomography (Cukjati et al. 2019). However, the use of the GBCD as the framework for boundary investigations has been overlooked. In this contribution, we investigate the relationship between grain boundary disorientation (hereafter used to indicate the minimum angular misorientation between adjacent grains, Wheeler et al. 2001) and interfacial segregation within a single olivine grain of a natural peridotite deformed by crystal plastic deformation. We analyze a set of low-angle boundaries with similar boundary geometries that exhibit small disorientation angle variations from 1.3° to 8° . By so doing, we investigate a small, but important region of GBCD related to the formation of low-angle boundaries. Our results represent the first, systematic, three-dimensional analysis of trace element segregation associated with dislocations migration during the formation of low-angle boundaries in naturally deformed olivine. The study provides a significant advance in our understanding of element mobility and segregation processes during deformation by subgrain rotation recrystallisation.

Geological settings and samples

The investigated samples were collected from a spinel-lherzolite found within the Lindås Nappe of the Bergen Arcs and located on the island of Holsnøy (SW Norway) (Fig. 1). The region comprises Neoproterozoic anorthositic granulites (930 ± 50 Ma, Austrheim and Griffin 1985, Boundy et al. 1992), with minor gabbroic components, mangerites, charnockites and ultramafic lenses (Austrheim 2013). Between

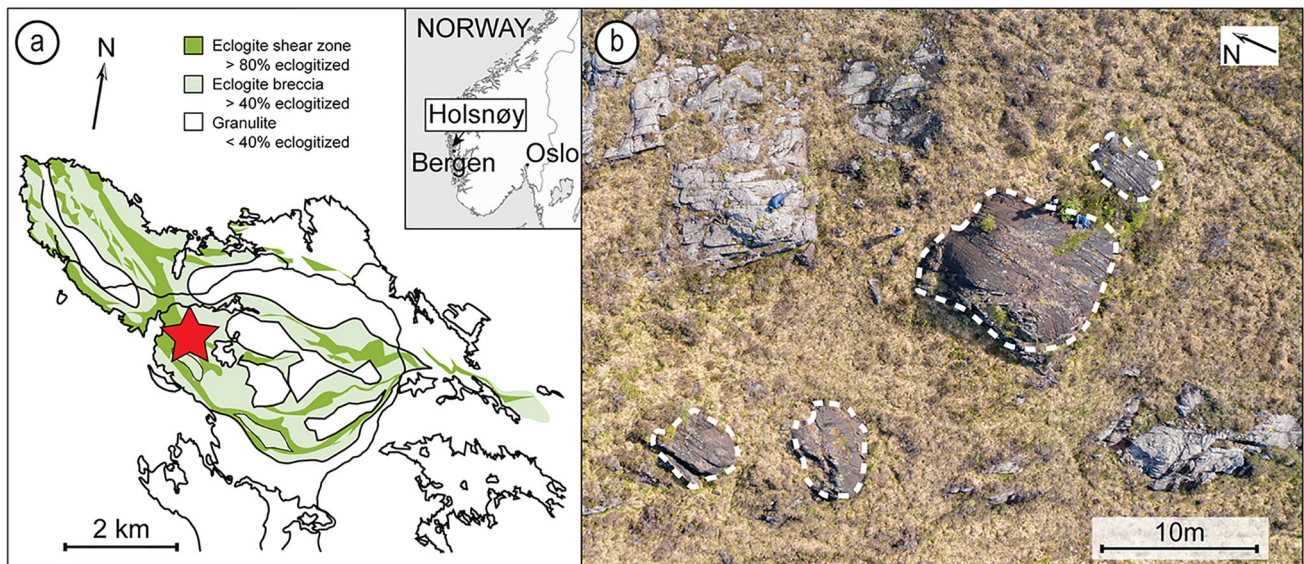


Fig. 1 **a** Simplified geological map of Holsnøy area (modified after Boundy et al. 1992). **b** Aerial photograph of the ultramafic lenses (dashed lines) outcrop

ca. 430 and 410 Ma, these rocks were locally overprinted at eclogite-facies conditions during a fluid infiltration event along fractures and shear zones (Austrheim and Griffin 1985; Bhowany 2018).

The spinel-lherzolites occur as localized lenses enclosed within the partially eclogitized anorthositic granulites and have been interpreted to represent the reworked product of pre-existing cumulate layers (Kühn et al. 2000) (Fig. 1). Within the spinel-lherzolites lenses, a well-developed compositional layering of olivine-pyroxene and garnet-rich bands lies broadly parallel to the granulite-facies foliation in the surrounding anorthositic granulites. The spinel-lherzolites contain abundant centimetre to millimetre wide high-strain zones that crosscut the dominant foliation (Fig. 2). Mineralogically, the metamorphic transition from the spinel- to garnet-lherzolite is indicative of upper mantle temperature and pressure conditions (O'Neill 1981). Moreover, the presence of minor hydrated minerals (e.g., amphibole) and dolomite are evidence of the presence of fluids during the deformation of these rocks (Kühn et al. 2000; Jung et al. 2014). Previous work on these high-strain zones has established that these features are related to the high-pressure Caledonian overprint (Kühn et al. 2000; Jung et al. 2014).

Methods

Secondary electron (SE), backscattered electron (BSE) and electron backscattered diffraction (EBSD) data were collected using a Tescan MIRA3 field emission scanning electron microscope (FESEM) housed at the John de Laeter Centre at Curtin University. EBSD data were acquired using

an Oxford Instrument Aztec system incorporating a Symmetry EBSD detector and Aztec 4.1 acquisition software using accelerating voltage of 20 kV at 20 mm working distance. EBSD maps were acquired using a step size of 0.5 μm , post-processed using Channel 5.12, and corrected utilizing a standard noise reduction procedure involving the removal of misindexed “wild spikes” and a six nearest-neighbour zero solution algorithm. Crystallographic orientation maps and pole figures were constructed using Tango and Mambo sub-components of Channel5 software, respectively. Geometrically necessary dislocation (GND) plots were performed using Aztec Crystal 1.1 software. Detected grains were defined using a critical disorientation of 22° based on molecular dynamic simulations of olivine boundary character (Adjaoud et al. 2012; Marquardt et al. 2015, 2018) and a minimum disorientation of 1° for boundary completion. Four grain boundaries were specifically selected for detailed atom probe tomography analysis based on similar geometries and disorientation axes. These boundaries have disorientation angles ranging between $\sim 1^\circ$ and $\sim 8^\circ$ and are inferred to have formed by similar processes arrested at different degrees of microstructural development.

Needle-shaped specimens for atom probe tomography (APT) and the electron-transparent thin foil for transmission electron microscopy (TEM) were prepared using a Tescan Lyra3 Ga⁺ Focused Ion Beam Scanning Electron Microscope (FIB-SEM) at the John de Laeter Centre at Curtin University. The four low-angle boundaries (LAB-1.3°, LAB-2.8°, LAB-4.5° and LAB-8°) were targeted for site-specific APT analysis using the “button” method described by Rickard et al. (2020). Additionally, during the entire sample

preparation procedure, the geometrical orientation of both the interfaces and the atom probe specimens were monitored to allow the reconstructed APT dataset to be geometrically linked to the boundary trace. Before APT analyses, a final 5 kV polishing stage was performed on all the prepared atom probe specimens to reduce Ga⁺ implantation and ion beam damage.

All APT specimens were analysed on a CAMECA LEAP 4000X HR at the Geoscience Atom Probe Facility (John de Laeter Centre, Curtin University) using a base temperature of 50–60 K, an ultraviolet laser ($\lambda = 355$ nm) with 80–150 pJ pulse energy, 200 kHz frequency and detection rate of 0.008 ions/pulse. Details of the APT technique are provided elsewhere (Reddy et al. 2020). The resulting time-of-flight mass/charge ratio spectra were processed and reconstructed in 3D using Cameca's IVAS 3.8.2 software. For the time-of-flight mass spectrum, the mass resolving power ($M/\Delta M$) between 1006 and 1096 was measured on the ²⁴Mg²⁺ ($M = 11.99$) peak. The peaks identified within each mass/charge ratio spectrum were compared to the local background and those with peak intensities that were twice above the background level were ranged. Additional details of the acquisition, processing, and reconstruction parameters are provided in Table S1 (Blum et al. 2018). Concentration analysis of the enriched regions was performed using proximity histograms (proxigrams) (Hellman et al. 2000) calculated using the ion concentration (at %) of Ca

and Ti (Table 1). In order to minimize cross-contamination between enriched domains, the composition of the matrix was obtained using values contained within 3 nm of the most distal portions from each enriched interface. The composition of the low-angle boundaries was obtained interpolating the at % obtained from the proxigrams of the interface and the atomic counts within each enriched region. 2D chemical profiles were also used to identify the spatial distribution of the enriched elements along the captured interfaces within the atom probe specimens (Fig. S3). In order to estimate the volatile composition of the boundary, OH (17 Da) was quantified as proxy for the H distribution. The accuracy of the approach will be discussed later in this paper.

Bright field (BF) scanning transmission electron microscopy (STEM) and high-angle annular dark-field (HAADF) images of a thin (<200 nm) olivine foil were acquired at 200 kV using a FEI Talos FS200X field emission transmission electron microscope (TEM) housed in the John de Laeter Centre at Curtin University.

Results

Microstructural characterization of the shear zone

At thin section scale, the undeformed wall-rock is coarse-grained and dominated by larger crystals of olivine (<1 mm)

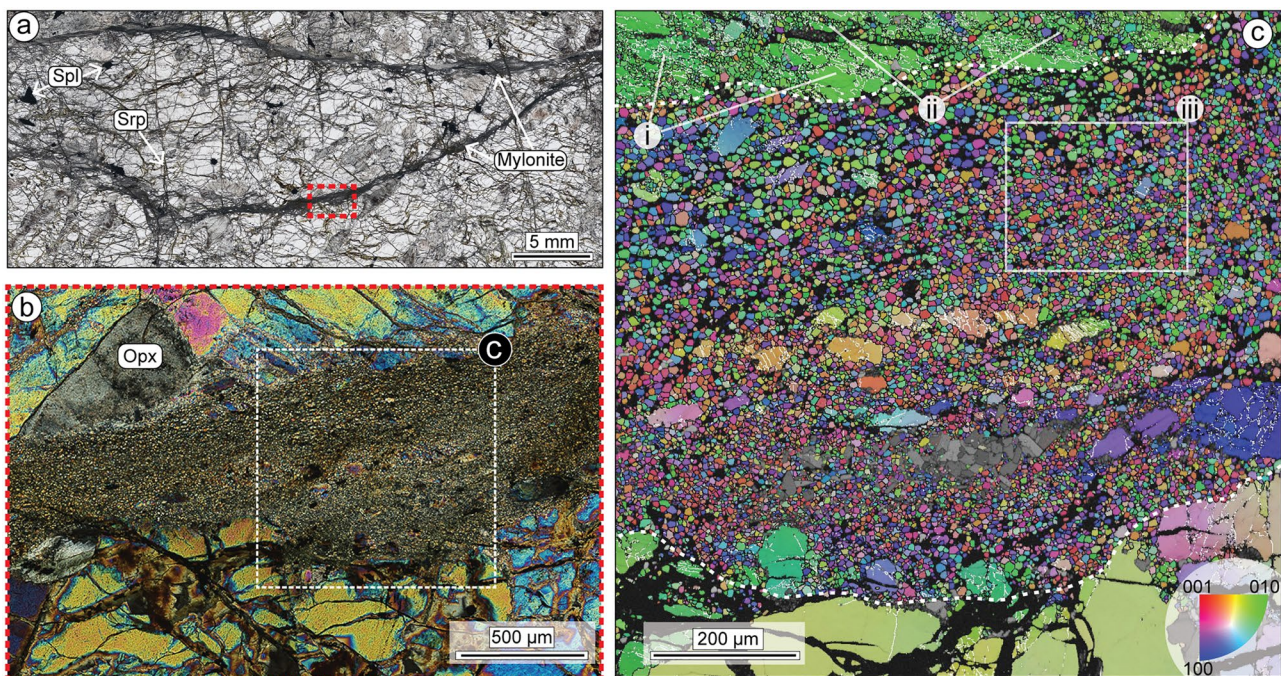


Fig. 2 **a** Optical plane-polarized photomicrograph of the investigated sample. Red box indicates the investigated EBSD site. Millimetre thick mylonites occur in separate regions of the sample. **b** Crossed-polarized photomicrographs of the investigated section of the lower

mylonite (red rectangle). White box represents the area of EBSD shown in **c**. **c** Inverse Pole Figure (IPF_v) EBSD map highlighting the differences in olivine grain orientations amongst the three different domains (i, ii, iii) of the shear zone. EBSD map step size 0.5 μm

together with ortho and clinopyroxene. Green spinel is widespread whereas amphibole and carbonates (mainly dolomite) occur as accessory minerals within the rock. Pyroxenes and spinel are often characterized by clusters of microscopic opaque exsolution resulting in a darker optical appearance. Serpentine alteration is present within the thin section, but is restricted to discrete cracks that crosscut the shear zones and host olivine grains (Fig. 2a).

The shear zones form an interconnected network of mm-wide, fine-grained, olivine-rich aggregates with minor orthopyroxene, clinopyroxene, amphibole, spinel and dolomite (Fig. 2a, b). The contact of the shear zone with the host varies from sharp to irregular with brecciated angular fragments of olivine and pyroxenes scattered within the mylonite matrix (Fig. 2b). Along the shear zone boundary, crystals of the wall-rock show deformation bands and undulose extinction under crossed polarized light. The transition to the fine-grained shear zone is highlighted by a marked decrease in grain-size (10–15 μm) and a visible variation in mineral orientations from the adjacent host-rock (Fig. 2b,

c). From the wall-rock towards the interior of the mylonite, three microstructurally distinct domains can be identified in the EBSD data (Fig. 2c).

Domain (i) represents the deformed host-rock olivine adjacent to the shear zone. Crystals of the host-rock contain low-angle boundaries accommodating small degrees of lattice distortion ($<22^\circ$) (Figs. 2c, 3). Two main trends of low-angle boundary directions can be distinguished, from upper-left to lower-right and from lower-left to upper-right, often intersecting at high angles (Fig. 3b). The pole figures show that the host-olivine grains of domain (i) are similarly oriented (Fig. 3b). Disorientation analysis of low-angle boundaries ($<22^\circ$) shows an alignment of disorientation axes with the [010] crystallographic direction (Fig. 3d).

Domain (ii) defines narrow regions that crosscut the host-grain of domain (i). This domain is characterized by the alternation of olivine and orthopyroxene rich bands with minor dolomite, spinel, and clinopyroxene (Fig. 3a, b). Domain (ii) is associated with a noticeable reduction in grain size ($<15 \mu\text{m}$ in diameter) and the development of olivine

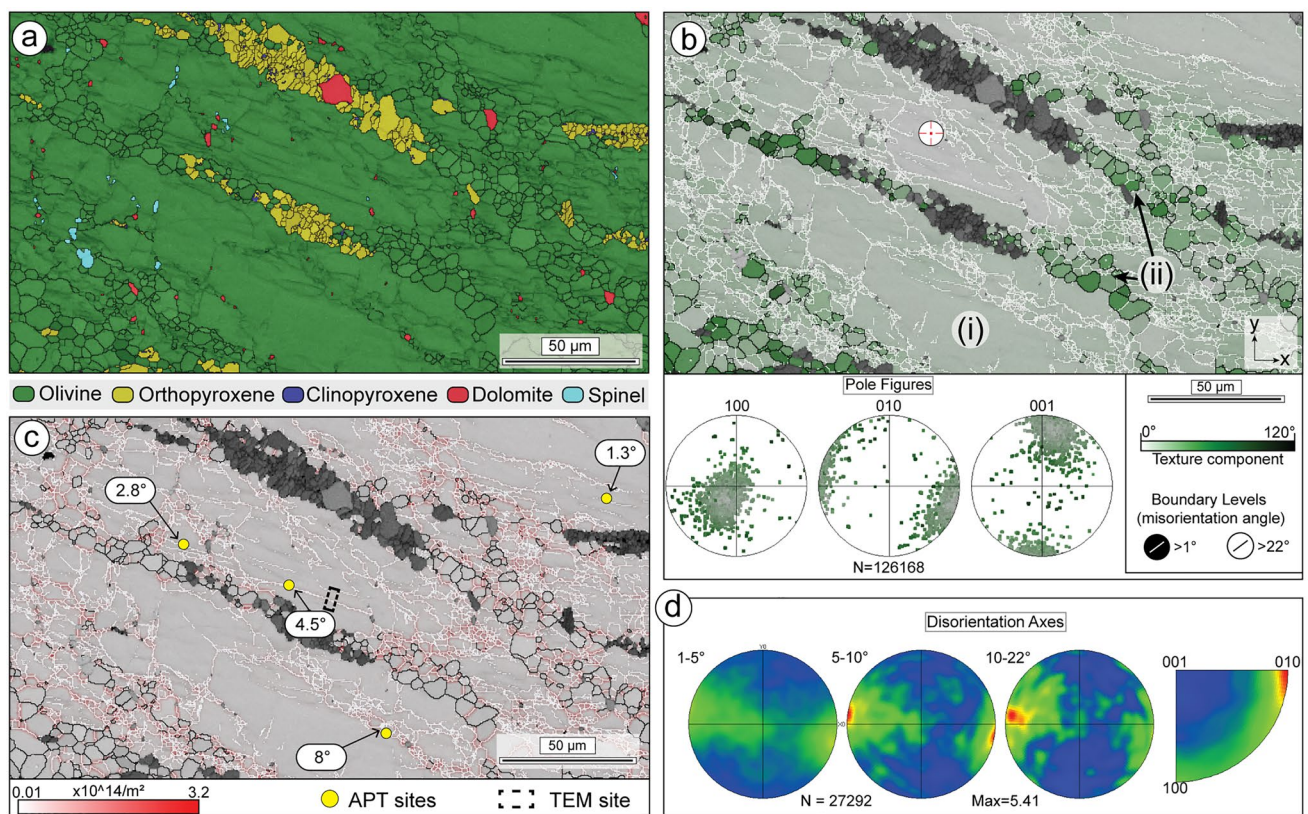


Fig. 3 Microstructural analysis of domain (i) and (ii) of the shear zone. Sample reference frame is shown in **b**. **a** Phase map obtained by automated EBSD mapping at 0.5 μm spacing. **b** Olivine grain reference orientation deviation map of domains (i) and (ii) obtained by EBSD mapping highlighting internal substructures of the deformed olivine of domain (i). Each pixel is colour-coded based on the deviation angle relative to the reference point indicated by a red cross in the map. Low-angle boundaries ($1\text{--}22^\circ$) are plotted in white, high-

angle boundaries ($>22^\circ$) in black. Pole figures for domain (i) and (ii) coloured for texture component are also shown. **c** GND density plot of [001] dislocation type. The map colour-scale refers to increasing dislocation densities. The location of the atom probe specimens and TEM analysis are also shown. **d** Disorientation axes plots in sample coordinates (left) and crystal coordinates (right) for the sub-grain boundaries ($<22^\circ$) of domain (i) and (ii)

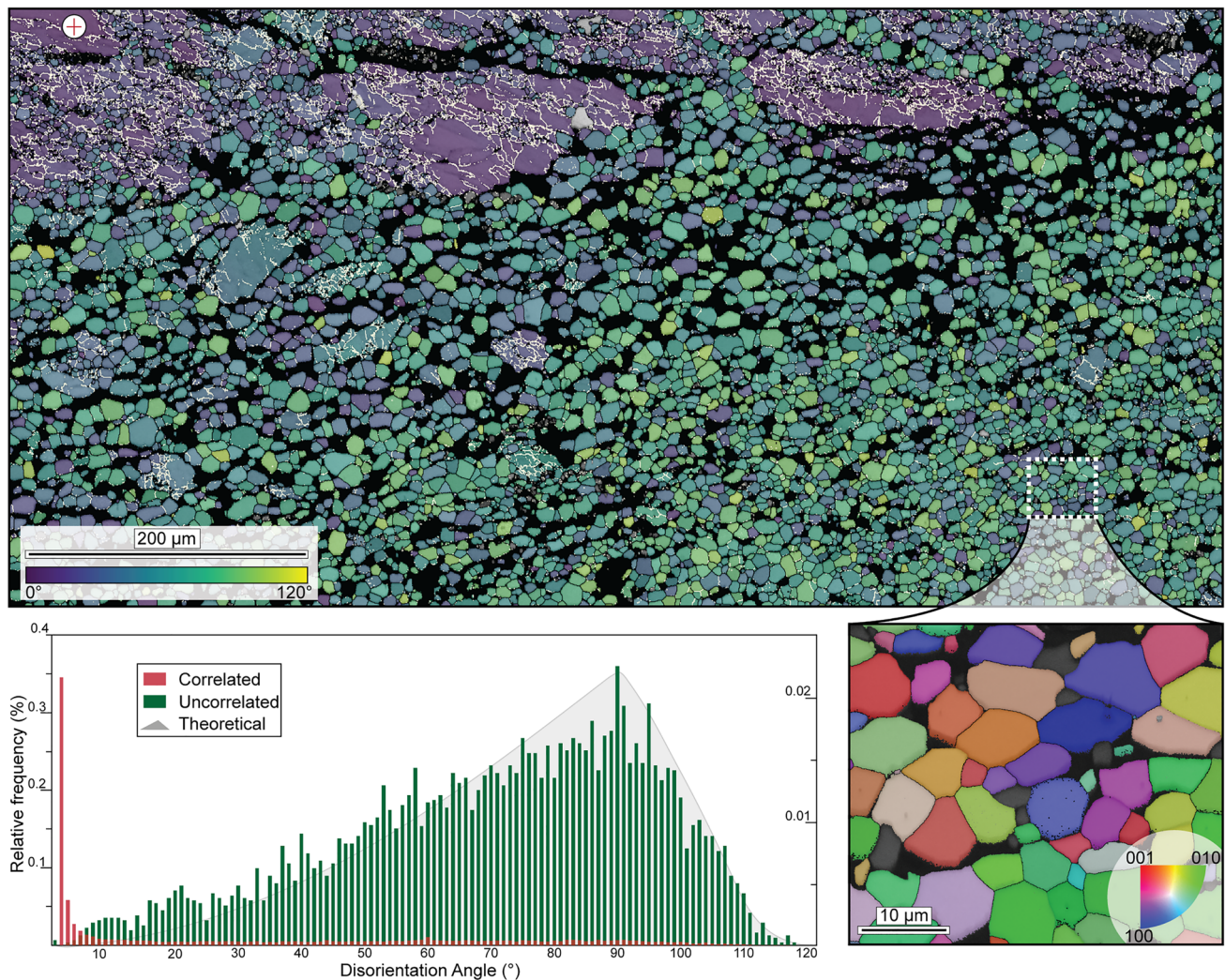


Fig. 4 EBSD orientation map of the upper part of the shear zone. Each pixel is colour-coded depending on olivine orientation from a reference point indicated with a red cross (upper left). Low-angle boundaries ($>1^\circ$) are indicated in white, high-angle boundaries ($>22^\circ$) in black. Bottom left: disorientation angle distribution for

correlated and uncorrelated disorientations. The grey area represents the theoretical random distribution. Bottom right: inverse pole figure (IPF_x) EBSD map highlighting the differences in olivine grain orientations within the mylonite and the presence of ca. 120° triple junctions. Map step size 50 nm

neoblasts distinguished by high-angle boundaries ($>22^\circ$). The neoblastic olivine grains are progressively reoriented from the host lattice orientation of domain (i) and until they become independent grains surrounded by high-angle boundaries $>22^\circ$ (Fig. 3b).

Domain (iii) represents the fine polycrystalline aggregate of the mylonite. The matrix is mainly formed by polygonal olivine grains (10–15 μm in diameter) with 120° triple junctions that show no significant internal misorientation variations (Figs. 2c, 4). Within this domain, larger grains of olivine (up to 50 μm in long dimension) record undulose extinction and internal subgrains that appear similar to those observed in domain (i). Analysis of uncorrelated disorientation angles within the shear

zone olivine shows them to be similar to the theoretical random distribution (Fig. 4). Correlated disorientation angles show a peak at $<10^\circ$ (Fig. 4). Using a 1° bin size, a fabric strength (M index) of 0.082 is calculated for 6802 grains in the shear zone (Skemer et al. 2005). These patterns are consistent with the analysis of weakly oriented neoblastic grains containing a small component of incompletely recrystallised grains inherited from the original host [domain (i)] (Figs. 2c, 4). Crystal aggregates of Cl-bearing amphibole are also present in localized portions of the shear zone whereas individual dolomite, pyroxenes, and spinel grains are scattered within the mylonite matrix.

To characterize the representative low-angle boundaries for atom probe tomography, the patterns of crystallographic

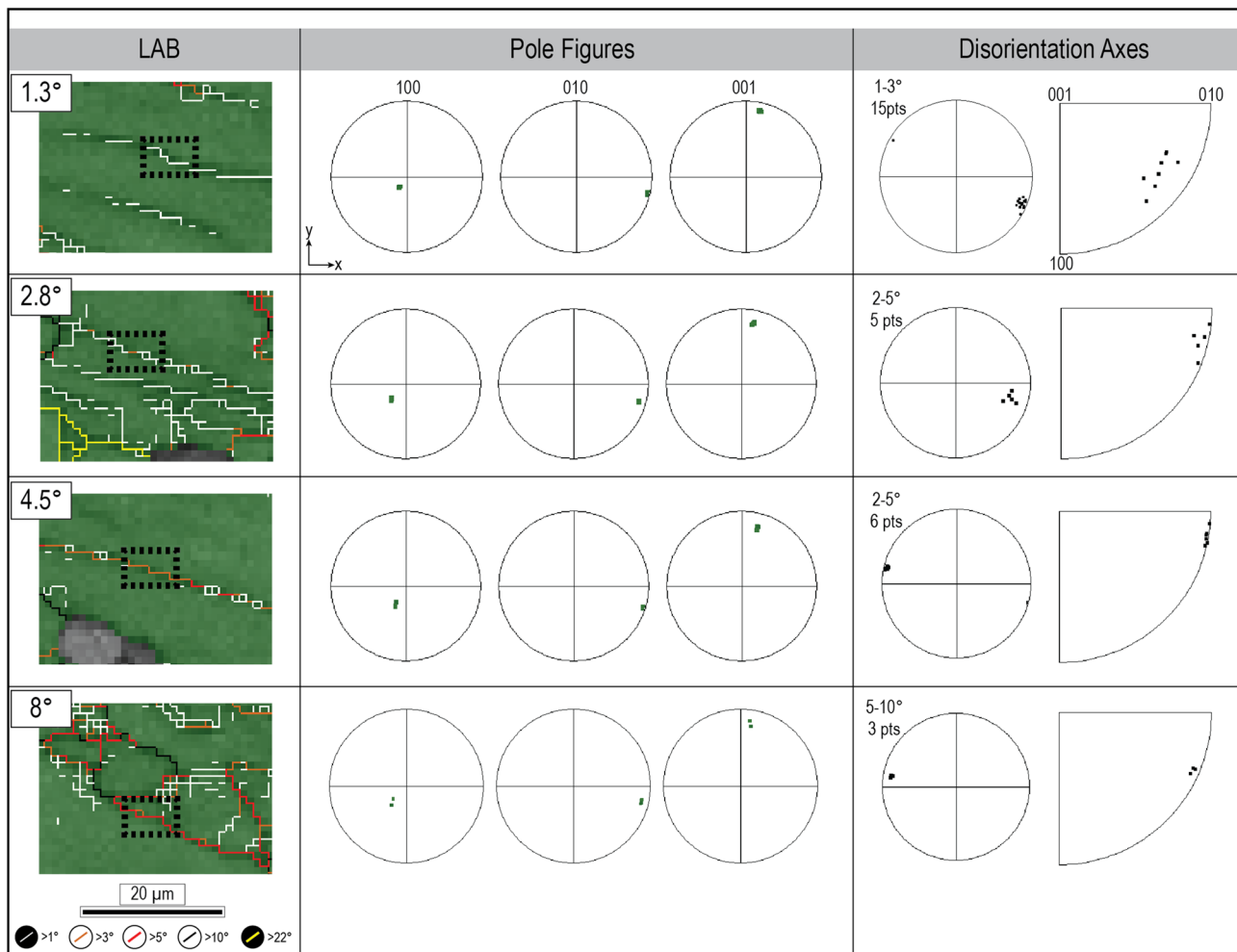


Fig. 5 Summary of EBSD phasemap (left) and stereographic projections (right) of the investigated low-angle boundaries. Black boxes in the EBSD maps show the subset for the pole figures plots and locations of atom probe tomography specimens lift-out. Grain boundaries

are colour-coded based on the degree of disorientation as displayed in the legend. Disorientation axes are displayed both in sample and crystal coordinates

orientation from EBSD data from domain (i) were combined with the geometry of the low-angle boundary trace to infer the slip system responsible for the formation of the observed low-angle boundary (Lloyd et al. 1997; Reddy et al. 2007). The dominant set of low-angle boundaries (upper-left to lower-right trending) shows disorientation axes that are aligned with the [010] crystallographic direction (Fig. 5). For tilt boundaries, the disorientation axis lies parallel to orientations of dislocations responsible for the lattice distortion. For [010] dislocations and the boundary trace observed in the EBSD maps, there are two possible olivine slip systems (e.g., (100)[001] and (001)[100]). Discrimination between these two possibilities is possible if the geometry of the boundary in the third dimension is known. This additional information can be found in the 3D APT reconstructions, but was also obtained from a TEM foil across the representative LAB-4.5° (Fig. 6). The analysis of the lamella

on the TEM revealed a complex network of ordered dislocations arranged along two perpendicular principal directions in the foil, a steeply dipping upper-right to lower-left and a shallower upper-left to lower-right directions (Fig. 6). These steep and shallow orientations within the foil are consistent with the operation of both the (100)[001] and (001)[100] slip systems, respectively. The analysed LAB-4.5° low-angle boundary was taken from the steeply dipping (ca. 70°) boundary and is consistent with formation by (100)[001] slip (Fig. 6). For the other analysed boundaries (LAB-1.3°, LAB-2.8° and LAB-8°), the geometry of the interface was measured from the atom probe tomography data, using a similar principle.

Atom probe tomography

Of the 22 olivine specimens analysed by APT, 10 yielded sufficient data for meaningful analysis. The mass spectra obtained from each of these ten specimens are all similar and record field evaporation of single ions and molecular species at a variety of charge states (Fig. S1). The bulk compositions of the reconstructed needles are consistent with the analysis of olivine (Table 1). The majority of the mass/

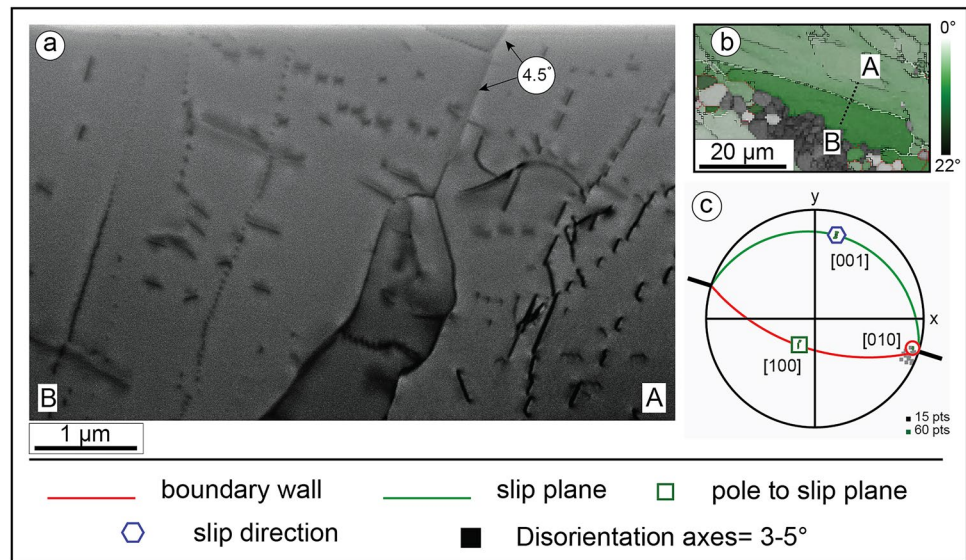
charge peaks represent the major elements present within olivine with trace elements forming minor peaks. 3D reconstruction of the APT data reveals the presence of linear and planar domains enriched in particular trace elements compared to the host olivine. Geometrically, the linear domains are broadly consistent with dislocation geometries inferred from the EBSD data, whilst planar domains are consistent with the expected orientation of the targeted steeply dipping low-angle boundaries (Fig. 7). Proxigrams obtained

Table 1 Composition of the different olivine specimens and low-angle boundaries obtained from APT

Element	LAB-1.3°				LAB-2.8°			
	Olivine	σ	Boundary	σ	Olivine	σ	Boundary	σ
O	47.52	0.06	46.04	0.82	46.85	0.08	46.08	1.23
Si	20.98	0.05	21.15	0.55	20.97	0.07	21.17	0.83
Fe	1.75	0.01	2.30	0.18	1.95	0.02	2.34	0.28
Mg	28.91	0.05	28.37	0.64	29.47	0.08	29.17	0.97
Ca	0.001	0.0002	0.34	0.07	0.001	0.0004	0.05	0.04
Al	0.44	0.01	0.69	0.10	0.41	0.01	0.51	0.13
Mn	0.12	0.004	0.21	0.05	0.12	0.01	0.19	0.08
Ti	0.02	0.002	0.17	0.05	0.02	0.002	0.18	0.08
Na	0.003	0.001	0.01	0.01	0.005	0.001	0.01	0.02
Cl	0.002	0.0004	0.23	0.06	0.001	0.0004	0.03	0.03
P	0.01	0.001	0.08	0.03	0.01	0.001	0.04	0.03
Co	0.02	0.001	0.03	0.02	0.01	0.002	0.03	0.03
H	0.16	0.005	0.31	0.07	0.14	0.01	0.16	0.07
Li	0.001	0.0003	0.001	0.003	0.001	0.0004	0.001	0.01
Ni	0.04	0.002	0.04	0.02	0.04	0.003	0.05	0.04
Cr	0.01	0.001	0.01	0.01	0.01	0.002	0.01	0.02
Sc	0.005	0.001	0.01	0.01	0.002	0.01	0.004	0.01
Element	LAB-4.5°				LAB-8°			
	Olivine	σ	Boundary	σ	Olivine	σ	Boundary	σ
O	46.02	0.11	45.76	0.83	47.39	0.05	46.38	0.41
Si	20.62	0.09	20.77	0.56	21.05	0.04	20.94	0.28
Fe	1.38	0.03	1.59	0.16	1.90	0.01	2.32	0.09
Mg	31.24	0.10	30.46	0.68	28.83	0.04	28.51	0.32
Ca	0.004	0.001	0.14	0.05	0.001	0.0001	0.23	0.03
Al	0.46	0.01	0.58	0.09	0.43	0.01	0.63	0.05
Mn	0.13	0.01	0.20	0.06	0.13	0.003	0.19	0.03
Ti	0.02	0.003	0.14	0.05	0.02	0.001	0.18	0.03
Na	0.003	0.001	0.01	0.01	0.004	0.001	0.01	0.01
Cl	0.002	0.001	0.06	0.03	0.003	0.0003	0.12	0.02
P	0.01	0.002	0.06	0.03	0.02	0.001	0.06	0.01
Co	0.01	0.002	0.02	0.02	0.02	0.001	0.03	0.01
H	0.05	0.005	0.18	0.05	0.15	0.003	0.31	0.03
Li	0.002	0.001	0.001	0.004	0.001	0.0003	0.001	0.002
Ni	0.03	0.004	0.03	0.02	0.04	0.002	0.05	0.01
Cr	0.01	0.002	0.01	0.01	0.01	0.001	0.01	0.01
Sc	0.003	0.001	0.004	0.01	0.003	0.0004	0.01	0.005

Concentrations are expressed in atomic %

Fig. 6 a HAADF STEM image of olivine lamella obtained across LAB-4.5°. The cross section shows the complexity of domain (i) microstructures. Two main directions of dislocations are distinguishable. **b** GROD-angle orientation map and TEM foil lift-out location (dashed black line). **c** Lower hemisphere and equal area projection of the crystallographic poles of LAB-4.5°. The boundary trace is shown by a thick black line outside the primitive circle. The red curve represents the boundary wall inferred by the tilt-boundary geometry of the low-angle boundary. The green curved line represents the slip plane (steeply dipping towards **B**) where the [001] represents the slip direction



from iso-concentration surfaces of the enriched domains show both enrichment and depletion in elements that are not clearly visible in the 3D maps (Figs. 8, S4).

Specimen LAB-1.3° showed a complex boundary geometry. The boundary is characterized by a planar feature constituted by a minimum of three visible sets of linear features intersecting at different angles. These linear features are decorated by Ca, Al, Ti, P, Cl and OH (Figs. 7, 8). The distribution of the enriched elements is heterogeneous as showed by 2D distribution profiles with increasing element concentrations at intersections of the linear features (Fig. S3). In particular, a strong increase is visible for Ca up to ca. 0.34 at %, Cl ca. 0.23 at %, Ti ca. 0.17 at %, P ca. 0.08 at % and OH ca. 0.31 at % followed by a depletion in O. Mg records a slight decrease in the bulk concentration but displays a positive detectable increment at the very inner side of the interface (Table 1, Fig. S4).

Specimen LAB-2.8° contains a main feature highlighted by the local enrichment of Ca (ca. 0.05 at %), Al (ca. 0.51 at %), Ti (ca. 0.18 at %), P (ca. 0.04 at %), Cl (ca. 0.03 at %) and Fe, and depletion of O and Mg (Fig. 7, Table 1). The lower zone is also associated with a set of linear features intersecting at a high angle (Fig. 7).

Within LAB-4.5°, the boundary is defined by equally spaced arrays of linear features oriented perpendicular to the vertical axis of the needle tip (Fig. S2). The interface is enriched in Ca, Al, Ti, P, Cl, Mn, Fe and OH (Figs. 7, 8). At the interface, Ca shows concentrations of ca. 0.14 at %, Al ca. 0.58 at %, Cl ca. 0.06 at %, Mn ca. 0.20 at % and OH 0.18 at %. A decreasing trend of concentration is displayed by Mg and O (Figs. 8, S4, Table 1).

The interface in specimen LAB-8° comprises numerous elongated features and these define a well-developed planar structure (Figs. 7, S2). The interface shows additional

enrichment of Na (ca. 0.01 at %) and Co (ca. 0.03 at %). Notably, the concentrations of the segregated elements are higher compared to LAB-2.8° and LAB-4.5°, with Ca up to ca. 0.23 at %, Al (ca. 0.63 at %), Cl (ca. 0.12 at %) and OH (ca. 0.31 at %) (Fig. 8, Table 1). Mg, Si and O are reduced within the boundary (Table 1, Fig. S4).

Discussion

Microstructural evolution of the olivine mylonite

EBSD orientation data are key to discriminate between different microstructural domains of the shear zone and determine the slip system responsible for the formation of the targeted interfaces for atom probe tomography analysis. In particular, three different microstructurally distinct domains (i, ii, iii) were distinguished showing a systematic increase in disorientation angle associated with the progressive recrystallization of the original host olivine (Figs. 3, 4).

The microstructures associated with domain (i) and domain (ii) are characterized by the development of sub-grain boundaries, grain size decrease, and a change in the character of crystallographic orientations. In particular, a higher density of low-angle boundaries, is apparent in areas adjacent to regions of neoblasts (Fig. 3b), in agreement with GND density in the order of 10^{14} m^{-2} (Fig. 3c). These features are consistent with domain (i) and domain (ii) having formed by the progressive migration and accumulation of dislocations into tilt boundary walls during crystal plasticity. The microstructures associated with the mylonite region [domain (iii)] are characterized by dislocation-free neoblasts displaying a near-random orientation distribution and the development of triple junctions at ca. 120° . This suggests

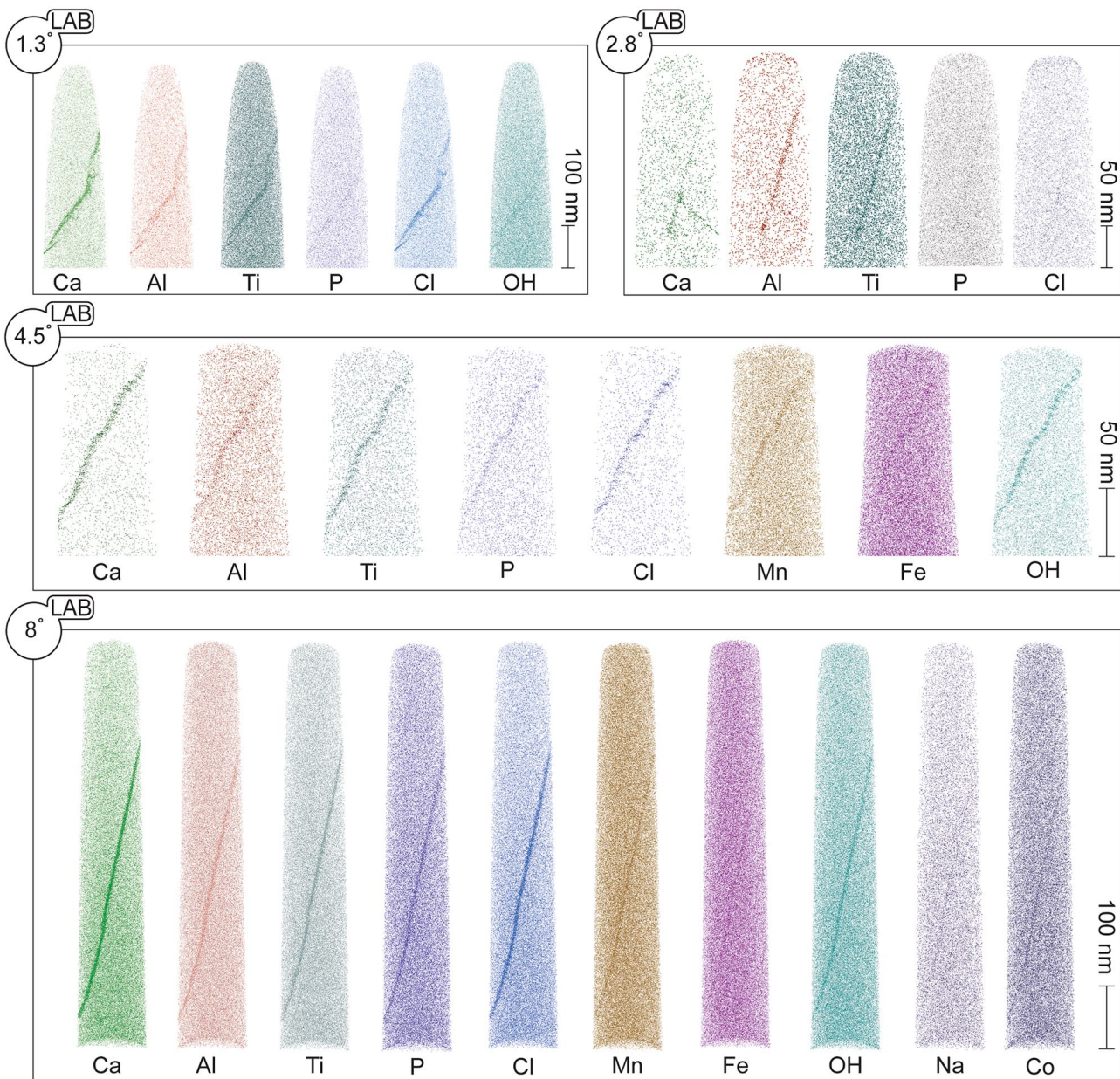


Fig. 7 3D reconstruction of atom probe specimens for LAB-1.3°, LAB-2.8°, LAB-4.5°, LAB-8°. Each dot in the atom map images represents one detected ionic species. Not all detected atoms are displayed for clarity. The maps show a distinct enrichment of incompat-

ible elements at the targeted interface. An increasing number of elements are found segregated at increasing degrees of disorientation associated with the same crystal slip system. Na and Co segregation is visible only at 8° disorientation angle

the occurrence of recrystallization during deformation and textural equilibrium associated with grain boundary migration within the shear zone. These observations indicate a progressive breakdown of the host olivine by dislocation creep and subgrain rotation recrystallization followed by a switch to grain size-sensitive creep (i.e. diffusion creep) within the shear zone.

The dominant deformation recorded within domain (i) is associated with low-angle boundary formation associated

with (100)[001] slip system. [001] slip system in olivine is relatively rare, with only a few natural examples having been recorded (Jung et al. 2013; Kaczmarek and Reddy 2013, and references therein). However, the operation of [001] slip in olivine has some important implications as it is preferentially activated during deformation associated with the presence of water and under modest to high-stress conditions (Jung and Karato 2001; Jung et al. 2006). In this study, the occurrence of low-angle boundaries dominated

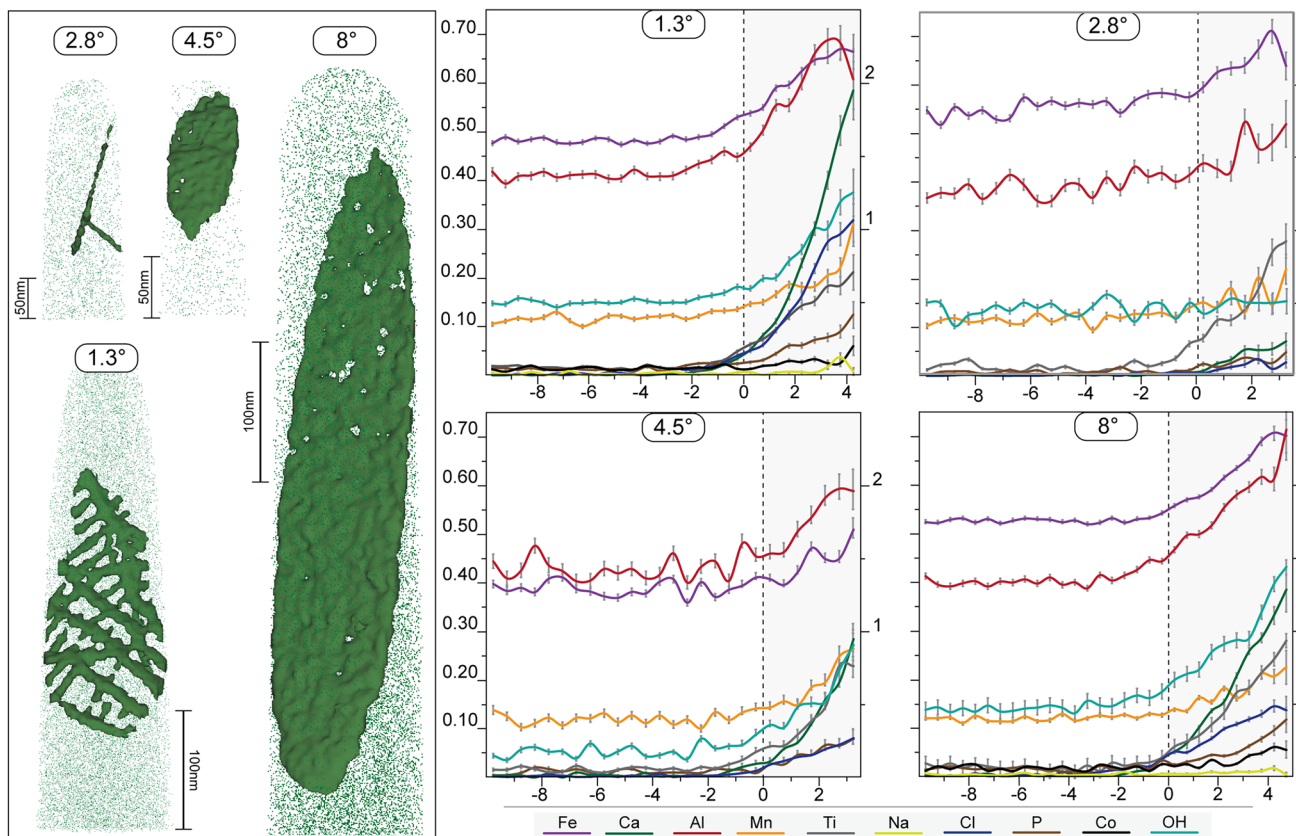


Fig. 8 3D isosurface renderings of the enriched region of the investigated low-angle boundary based on the concentration of Ca and Ti and relative proximity histogram profiles for visible segregated elements at the interface. The histograms show the gradual increase of

concentration expressed in at % for Ca, Al, Mn, Ti, Na, Cl, P, Co and OH (left y scale) and Fe (right y scale) from the edge (distance 0) towards the inner side of the interface. Distance is expressed in nm

by the activity of (100)[001] is therefore consistent with previous interpretations of the Holsnøy peridotites being deformed during the Caledonian orogeny by shear localization in the presence of fluids (Jung et al. 2014) and by the regional Caledonian eclogite-facies overprint being localised to zones of fluid infiltration (Austrheim 2013; Bhowany et al. 2018). The presence of recrystallized Cl-bearing amphibole aggregates and dolomite within the mylonite matrix further supports the presence of a fluid component during the deformation of these rocks.

The relationship between low-angle boundary disorientation, interface structure and trace element composition

A systematic assessment of the relationship between disorientation angle and composition of similarly oriented low-angle boundaries has been undertaken by site-specific atom probe targeting within the deformed host-olivine of domain (i). The atom probe data revealed the enrichment of multiple

trace elements (Ca, Al, Ti, P, Mn, Fe, Na, Co, Cl and OH) at these interfaces (Figs. 7, 8).

Three of the low-angle boundaries captured within the analysed specimens (LAB-2.8°, LAB-4.5° and LAB-8°) are characterized by relatively planar surfaces that are internally defined by equally spaced arrays of decorated linear features (Figs. 7, 8). Monitoring of orientation relationships between the thin section and the atom probe specimens during preparation and analysis enables the correlation of the geometrical features in the atom probe data with microstructural information collected from the thin section. This correlation indicates that the linear features within the boundary interfaces are parallel to the disorientation axes inferred from the EBSD analysis of the boundaries. Hence, we interpret these features to represent the preferential segregation of trace elements to dislocations within the low-angle boundaries. In detail, the morphology and distribution of the reconstructed iso-concentration surfaces for these specimens are consistent with the steeply dipping (100) boundary planes observed in the TEM data being internally defined by arrays of decorated

dislocations aligned parallel to the [010] olivine crystallographic direction (Fig. S2).

With the exception of LAB-1.3°, the low-angle boundaries LAB-2.8°, LAB-4.5° and LAB-8° display a positive correlation between disorientation angle and trace element enrichment (Fig. 8, Table 1). In detail, LAB-2.8° is enriched in Ca, Al, Ti, P, Cl. In addition to these, Mn, Fe and OH become visible at 4.5° of disorientation. Minor enrichment of Na and Co is only apparent in LAB-8° (Fig. 7). A concomitant progressive depletion in Mg (and O) is visible from LAB-2.8° to LAB-8° (Fig. S4, Table 1).

Conversely, at low degrees of lattice distortion, the framework of the boundary captured within LAB-1.3° specimen is defined by a more complex arrangement of elongated features intersecting at various angles, which are interpreted to represent the intersection of multiple dislocations aligned parallel to the [010], [001] and [011] olivine crystallographic directions (Fig. S2). The atomic concentrations of enriched elements registered within LAB-1.3° interface showed a poor correlation compared with the linear trend observed between LAB-2.8°, LAB-4.5° and LAB-8° (Table 1). In fact, the concentrations of commonly enriched trace elements within LAB-1.3° are the highest values across all of the analysed specimens. As observed from 2D chemical profiles for Ca, Cl and Ti, the distribution of the enriched elements within LAB-1.3° is heterogeneous with segregation preferentially localized at dislocation intersections (Fig. S3). Similar features have been observed in low-angle boundaries developed within zircon (Piazolo et al. 2016; Reddy et al. 2016) and pyrite (Fougerouse et al. 2019). In such cases, minor lattice distortion (< 3°) is insufficient to form ordered dislocation arrays and the entanglement of geometrically distinct dislocations is responsible for the local enrichment (i.e. clustering) of segregated elements (Fougerouse et al. 2019). It is well known from the Material Science literature that the increasing disorientation between adjacent subgrains corresponds to a decrease of the spacing between the lattice dislocations that constitute the subgrain boundary (Read and Shockley 1950; Frank 1951; Priester 2013). At higher lattice distortion, the individual dislocations contributing to the formation of a subgrain boundary gradually overlap, until the formation of high-angle boundaries is reached, in which the identification of singular dislocations is no longer possible. Therefore, one possible explanation of the increased trace element concentrations in LAB-1.3° is that, at really low-angle of disorientation, the dominant dislocation sets had no time to mature and the observed boundary structure and trace element enrichment represent the result of a mixture of different slip system required for plastic deformation of a single grain (“von Mises criteria”).

With the exception of the trace element concentrations within LAB-1.3°, which is complicated by the presence of multiple dislocation types, the quantitative geochemical data

strongly suggest the presence of a systematic relationship between the degree of lattice misorientation, the structure of the grain boundary, and the extent of trace element segregation at those interfaces.

Mechanisms of trace element segregation to low-angle boundaries

The enrichment of solute ions at mineral interfaces is a well-known phenomenon in manufactured material and is considered to reflect the minimization of the elastic strain energy derived by non-stoichiometric atoms within the crystal lattice and space charge compensation (Hondros and Seah 1977; Priester 2013). This enrichment can include mechanisms deriving from the ability of static dislocations to attract interstitial elements (“Cottrell atmosphere”, Cottrell and Bilby 1949) or the coupled mobility of trace elements with dislocations as they migrate towards low-angle boundaries during deformation (e.g. Reddy et al. 2006, 2007).

In this study, crystal plasticity accommodated by subgrain rotation recrystallization is interpreted to be responsible for the development of domains (i) and (ii) during deformation (Fig. 3). Apart from the boundary with the smallest disorientation angle, which is microstructurally distinct from the other studied low-angle boundaries due to the complexity in dislocation types, the boundaries show increasing trace element enrichment with increasing disorientation angle. The elements that are enriched in the boundaries show some similarities with the composition of high-angle grain boundaries in natural and experimentally deformed olivine (Ando 2001; Hiraga et al. 2002, 2003, 2004; Marquardt et al. 2015; Marquardt and Faul 2018; Cukjati et al. 2019). These elements are, by enlarge, trace elements that are found within natural olivine (De Hoog et al. 2010). The segregation of incompatible trace elements (e.g., Ca, Al and Ti) has been previously reported from studies of olivine grain boundaries, and it is mostly dictated by the bulk composition of the rock and the crystal chemistry (Hiraga et al. 2002, 2003, 2004; Marquardt and Faul 2018). Similar observations have also been reported in atom probe studies of low-angle boundaries in zircon and pyrite (Reddy et al. 2016; Piazolo et al. 2016; Fougerouse et al. 2019) and observation in metals and alloys also show an increase of trace element segregation with the number of accumulated dislocations within a boundary (Watanabe 1985).

HREM and AEM studies have demonstrated that local enrichment of particular elements can also be attributed to the occurrence of thin intergranular phases, such as amorphous layers or interstitial precipitates (e.g. Wirth 1996; Marquardt et al. 2015). In this study, however, the observation that elements segregation at low-angle boundary interfaces is followed by a concomitant depletion in elements, such as Si, O and Mg, indicates the preservation of olivine

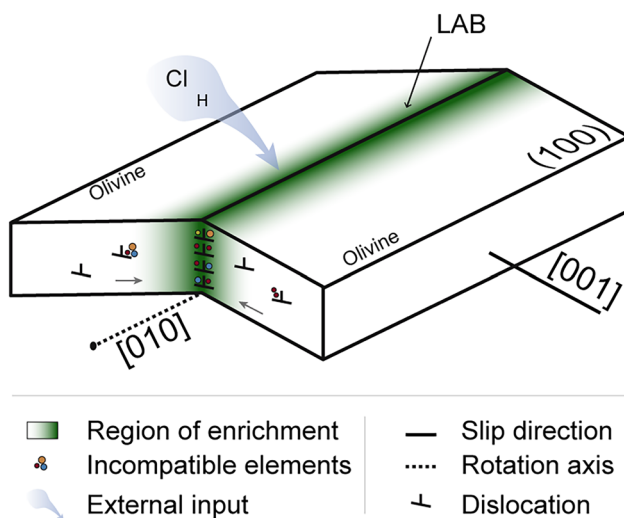


Fig. 9 Schematic representation of the proposed model of incompatible element segregation along the interface of a symmetric low-angle tilt boundary (modified after Reddy et al. 2007). The migration of dislocations facilitates the mobility of solute ions towards the low-angle boundary during deformation. The infiltration of Cl and H from an external fluid source is here represented by the blue arrow

stoichiometry (Hiraga et al. 2004). Moreover, the concentration of trace elements at the analysed interfaces does not exceed a few at %. This implies that, at the nanometre scale, the interface is still dominated by the typical olivine composition. These observations, therefore, allow us to exclude the presence of an independent intergranular phase between adjacent grains.

Based on EBSD and APT data, we interpret the enrichment of elements, such as Ca, Al, Ti, P, Mn, Fe, Na, and Co, to reflect the capture and migration of olivine-hosted trace elements in dislocations that migrate to the low-angle boundary during deformation. Our results are consistent with a dynamic and progressive migration and accumulation of dislocations at low-angle boundaries, the associated mobility of trace elements along with these migrating dislocations, and the equilibrium segregation of these trace elements at newly formed subgrain interfaces (Fig. 9). The site-specific targeting of low-angle boundaries characterized by a similar tilt boundary geometry provides information from a small, but important, subset of GBCD variables, and shows a systematic relationship between subgrain boundary disorientation and composition. Since the GBCD and interfacial segregation are two interlinked manifestations of grain boundary energy minimization, associated with both surface energy and impurity-related elastic strain, these results show the likelihood of a complex structure-property relationship between microstructure and grain boundary composition.

In addition to non-stoichiometric ions, the low-angle boundaries captured with APT are found to be enriched in Cl and OH. The evidence for a [001] slip and previous studies

on the same outcrops argue for shear zone formation in a fluid-present geochemical environment (Kühn et al. 2000; Austrheim 2013; Jung et al. 2014; Bhowany et al. 2018). Therefore, although concentrated along the targeted microstructures, there is the possibility that Cl and OH represent exotic components derived from the fluid phase. The presence of H^+ at the analysed interfaces (evaporated as hydroxide anion) is not trivial to assess with atom probe data. It is possible that detected H^+ may represent chamber-sourced hydrogen within the local evaporation field of the planar interfaces during the analysis. However, recent studies using coupled cryogenic sample preparation techniques and APT, have confirmed hydrogen segregation within crystal defects, including interfaces (Chen et al. 2020). Furthermore, since the occurrence of H^+ in olivine is strongly attributed to Ti point defects (Berry 2005; Walker et al. 2007; Demouchy and Alard 2021), the segregation of Ti to grain boundaries is consistent with the observed enrichment of hydrogen in the low-angle interfaces. Moreover, the concentration of hydrogen in the different boundaries is consistent with the systematic Ti enrichment observed within LAB-2.8°, LAB-4.5° and LAB-8°. The role of interfaces, formed during subgrain rotation recrystallization, as pathways for subsequent addition of externally derived trace elements has been shown by Pb isotope analysis intragrain boundaries in pyrite (Fougereuse et al. 2019). Therefore, considering the available dataset and both the geological and petrological context of the sample, we can speculate the Cl and H^+ signature detected within the low-angle boundaries to be real and reflecting an externally derived Cl-bearing fluid present during deformation (Fig. 9). The progressive increase of atomic concentrations of these trace elements with increasing disorientation may reflect increasingly easier diffusion in boundaries with higher dislocation densities.

Segregation of solute ions to grain boundaries and intergranular precipitation in response to variation in thermodynamic variables, such as decrease of temperature, is a well-known phenomenon in material science (Dillon et al. 2016). The cooling of the sample, for example, generates a decrease in solubility of incompatible trace elements within the crystal lattice and the less-ordered grain boundaries become energetically more favourable as sites of segregation (Priester 2013). The EBSD and APT data presented here indicate a systematic relationship between disorientation and trace element concentrations in the boundaries and there is no evidence for significant modification of low-angle boundary composition after their formation. Unlike many manufactured materials, the segregation of trace elements to grain boundaries in olivine may not represent a continuous equilibrium process during cooling, but may instead represent the composition shortly after boundary formation. This lack of exchange may reflect the inability of trace elements to migrate through the olivine lattice by volume diffusion once

deformation has ceased at temperatures < 700 °C (Cherniak and Liang 2014).

Geological implications

The microstructural and compositional analysis of low-angle boundaries in natural olivine presented in this study shows a previously unidentified structure-chemistry relationship between the amount of lattice distortion and trace element segregation. Although it is generally considered that grain boundaries in polycrystalline materials represent sites of preferential diffusion pathways, for example, being an order of magnitude faster than intracrystalline diffusion (Dohmen and Milke 2010), our data show that different amount of lattice disorientation in tilt boundaries, associated with the activity of the same slip system, leads to marked compositional differences within the boundary interface. Since element diffusion along 2-dimensional grain boundaries is strongly controlled by the chemistry of the interface (Wuensch and Vasilos 1966), then this has the potential to affect grain boundary diffusion, which in turn can affect viscosity properties (Marquardt and Faul 2018 and references therein) and diffusion rates (Priester 2011; Cukjati et al. 2019). Furthermore, the presence of solute atoms segregated at grain boundaries will modify the structure of the interface, thereby affecting the energy of the grain boundary, which is an important factor controlling the grain size of polycrystalline aggregates (Priester 2013; Hiraga et al. 2007). Grain size is a critical property of materials and controls deformation mechanisms and the properties of rocks during deformation. The nanoscale data presented in this study might therefore have the potential to yield important implications for the intrinsic properties of the rock during crystal plastic deformation, highlighting the importance of the geometry of grain boundary interfaces in controlling the migration of solute ions.

The localization of H^+ in the boundary interfaces within olivine has significant implications for the rheological properties of mantle rocks during deformation (Mei and Kohlstedt 2000). In addition, the heterogeneity of hydrogen within nominally anhydrous minerals, such as olivine, can drastically affect physico-chemical properties of the aggregate. The distribution of hydrogen at grain boundaries will have major consequences of decreasing the strength in dislocation and diffusion creep regime (Mei and Kohlstedt 2000), facilitate and promote chemical reactions and phase transitions, and will modify geophysical properties, such as electrical conductivity (Wang et al. 2006) and seismic energy attenuation (Karato and Jung 1998).

Previous studies investigating compositional variations associated with low-angle boundaries have suggested that variation in the Fe content of olivine can play an important control in localizing phase transformations in the mantle,

which may promote seismicity within deeply subducted lithosphere (Ando 2001). This previous study utilized electron beam techniques to show variations at the scale of ~ 200 nm (Ando 2001). The obtained APT data in this study show that variations in Fe content associated with low-angle boundaries is at a much-finer scale than previously measured—only restricted to a few nanometres. The results also show that Fe enrichment is heterogeneous within these grain boundaries, generally segregating to dislocations within the boundary interface. Moreover, these observations may also imply that phase transformation of olivine, facilitated by Fe heterogeneity, can affect the strength of the upper mantle at early stages of deformation without requiring the application of high differential stress.

Conclusions

The characterization of the nanostructure and chemistry of low-angle boundaries in olivine obtained by atom probe tomography provides unprecedented evidence of trace elements segregation to low-angle boundary interfaces during deformation. This study reports a direct positive correlation between disorientation angle and the degree of interfacial segregation of solute ions. In addition, the results show a relationship between the composition of low-angle boundaries and the level of grain boundary complexity. The process of segregation identified in this study involves the capture and the transportation of solute ions within mobile dislocations. Potentially exotic trace elements, such as Cl and H, likely reflect a small, but significant, contribution of an external fluid source also being localized along the grain boundaries. The compositional variations associated with low-angle boundaries have implications for grain deformation and phase transformation of olivine in the deep Earth as well as interpretation of geophysical data, such as electrical conductivity and seismic energy attenuation.

Supplementary Information The online version contains supplementary material available at <https://doi.org/10.1007/s00410-021-01815-3>.

Acknowledgments The authors gratefully acknowledge constructive comments from T. Hiraga and an anonymous reviewer which helped improve the quality of the manuscript. We thank D. Canil for the editorial handling and valuable comments that helped improve the final version. The corresponding author owes personal thanks to Joseph C. for helpful discussions.

Authors' contributions According to CRediT (Contributor Roles Taxonomy). Tommaso Tacchetto: conceptualization, methodology, investigation, visualization, writing—original draft, Steven M. Reddy: supervision, conceptualization, methodology, writing—review and editing. David W. Saxey: supervision, visualization, writing—review and editing. Denis Fougereuse: formal analysis, writing—review and Editing. William D. A. Rickard: formal analysis, writing- review and

editing. Chris Clark: supervision, conceptualization, resources, writing—reviewing and editing, funding acquisition.

Funding This work was supported by the Australian Research Council support (LP130100053, DP160104637 and DP210102625). The Geoscience Atom Probe and FIB-SEM facilities at Curtin University were developed under the auspices of the National Resource Sciences Precinct (NRSP), a collaboration between Curtin University, CSIRO and the University of Western Australia, supported by the Science and Industry Endowment Fund (SIEF RI13-01), and are now maintained in Curtin University's John de Laeter Centre.

Data availability material All data and material used and discussed in the text are included as Figures and Tables in the main text or as Supplementary Material.

Declarations

Conflict of interests The authors declare that they have no known competing financial interests or personal relationships that could have appeared to influence the work reported in this paper.

References

- Adjaoud O, Marquardt K, Jahn S (2012) Atomic structures and energies of grain boundaries in Mg_2SiO_4 forsterite from atomistic modeling. *Phys Chem Miner* 39:749–760. <https://doi.org/10.1007/s00269-012-0529-5>
- Ando J, Shibata Y, Okajima Y et al (2001) Striped iron zoning of olivine induced by dislocation creep in deformed peridotites. *Nature* 414:893–895. <https://doi.org/10.1038/414893a>
- Austrheim H (2013) Fluid and deformation induced metamorphic processes around moho beneath continent collision zones: examples from the exposed root zone of the Caledonian mountain belt, W-Norway. *Tectonophysics* 609:620–635. <https://doi.org/10.1016/j.tecto.2013.08.030>
- Austrheim H, Griffin WL (1985) Shear deformation and eclogite formation within granulite facies anorthosites of the Bergen Arcs, western Norway. *Chem Geol* 50:267–281
- Berry AJ, Hermann J, O'Neill HSC, Foran GJ (2005) Fingerprinting the water site in mantle olivine. *Geology* 33:869. <https://doi.org/10.1130/G21759.1>
- Bhowany K, Hand M, Clark C et al (2018) Phase equilibria modelling constraints on P-T conditions during fluid catalysed conversion of granulite to eclogite in the Bergen Arcs, Norway. *J Metamorph Geol* 36:315–342. <https://doi.org/10.1111/jmg.12294>
- Blum TB, Darling JR, Kelly TF et al (2018) Best practices for reporting atom probe analysis of geological materials. In: Moser DE, Corfu F, Darling JR et al (eds) *Geophysical Monograph Series*. Wiley, Hoboken, NJ, USA, pp 369–373
- Boudry TM, Fountain DM, Austrheim H (1992) Structural development and petrofabrics of eclogite facies shear zones, Bergen Arcs, western Norway: implications for deep crustal deformational processes. *J Metamorph Geol* 10:127–146
- Chen Y-S, Lu H, Liang J et al (2020) Observation of hydrogen trapping at dislocations, grain boundaries, and precipitates. *Science* 175(2020):171–175
- Cherniak DJ, Liang Y (2014) Titanium diffusion in olivine. *Geochim Cosmochim Acta* 147:43–57. <https://doi.org/10.1016/j.gca.2014.10.016>
- Cottrell AH, Bilby BA (1949) Dislocation theory of yielding and strain ageing of iron. *Proc Phys Soc A* 62:49–62. <https://doi.org/10.1088/0370-1298/62/1/308>
- Cukjati JT, Cooper RF, Parman SW et al (2019) Differences in chemical thickness of grain and phase boundaries: an atom probe tomography study of experimentally deformed wehrilite. *Phys Chem Miner* 46:845–859. <https://doi.org/10.1007/s00269-019-01045-x>
- De Hoog JCM, Gall L, Cornell DH (2010) Trace-element geochemistry of mantle olivine and application to mantle petrogenesis and geothermobarometry. *Chem Geol* 270:196–215. <https://doi.org/10.1016/j.chemgeo.2009.11.017>
- Demouchy S, Alard O (2021) Hydrogen, trace, and ultra-trace element distribution in natural olivines. *Contrib Mineral Petrol* 176:26. <https://doi.org/10.1007/s00410-021-01778-5>
- Dillon SJ, Tai K, Chen S (2016) The importance of grain boundary complexions in affecting physical properties of polycrystals. *Curr Opin Solid State Mater Sci* 20:324–335. <https://doi.org/10.1016/j.cossms.2016.06.003>
- Dohmen R, Milke R (2010) Diffusion in polycrystalline materials: grain boundaries, mathematical models, and experimental data. *Rev Mineral Geochem* 72:921–970. <https://doi.org/10.2138/rmg.2010.72.21>
- Faul UH, Fitz Gerald JD, Jackson I (2004) Shear wave attenuation and dispersion in melt bearing olivine polycrystals 2 microstructural interpretation and seismological implications. *J Geophys Res.* <https://doi.org/10.1029/2003JB002407>
- Fougerouse D, Reddy SM, Kirkland CL et al (2019) Time-resolved, defect-hosted, trace element mobility in deformed Witwatersrand pyrite. *Geosci Front* 10:55–63. <https://doi.org/10.1016/j.gsf.2018.03.010>
- Frank FC (1950) The resultant content of dislocations in an arbitrary intercrystalline boundary. In: *Symposium on The Plastic Deformation of Crystalline Solids*, Mellon Institute, Pittsburgh, (NAVEXOS-P-834), p 150
- Hakon A, Griffin WL (1985) Shear deformation and eclogite formation within granulite-facies anorthosites of the Bergen Arcs, western Norway. *Chem Geol* 50:267–281
- Hansen LN, Zimmerman ME, Kohlstedt DL (2012) The influence of microstructure on deformation of olivine in the grain-boundary sliding regime: Effect of microstructure on deformation. *J Geophys Res Solid Earth.* <https://doi.org/10.1029/2012JB009305>
- Hellman OC, Vandenbroucke JA, Rüsing J et al (2000) Analysis of three-dimensional atom-probe data by the proximity histogram. *Microsc Microanal* 6:437–444. <https://doi.org/10.1007/S100050010051>
- Hiraga T, Anderson I, Zimmerman M et al (2002) Structure and chemistry of grain boundaries in deformed, olivine + basalt and partially molten lherzolite aggregates: evidence of melt-free grain boundaries. *Contrib Miner Petrol* 144:163–175. <https://doi.org/10.1007/s00410-002-0394-1>
- Hiraga T, Anderson IM, Kohlstedt DL (2003) Chemistry of grain boundaries in mantle rocks. *Am Miner* 88(6976):1015–1019
- Hiraga T, Anderson IM, Kohlstedt DL (2004) Grain boundaries as reservoirs of incompatible elements in the Earth's mantle. *Nature* 427(6976):699–703
- Hiraga T, Hirschmann MM, Kohlstedt DL (2007) Equilibrium interface segregation in the diopside–forsterite system II: applications of interface enrichment to mantle geochemistry. *Geochim Cosmochim Acta* 71:1281–1289. <https://doi.org/10.1016/j.gca.2006.11.020>
- Hondros ED, Seah MP (1977) Segregation to interfaces. *Int Metals Rev* 22:262–301. <https://doi.org/10.1179/imtr.1977.22.1.262>
- Jung H, Karato S-I (2001) Effects of water on dynamically recrystallized grain-size of olivine. *J Struct Geol* 23:1337–1344

- Jung H, Katayama I, Jiang Z et al (2006) Effect of water and stress on the lattice-preferred orientation of olivine. *Tectonophysics* 421:1–22. <https://doi.org/10.1016/j.tecto.2006.02.011>
- Jung H, Lee J, Ko B et al (2013) Natural type-C olivine fabrics in garnet peridotites in North Qaidam UHP collision belt, NW China. *Tectonophysics* 594:91–102. <https://doi.org/10.1016/j.tecto.2013.03.025>
- Jung S, Jung H, Austrheim H (2014) Characterization of olivine fabrics and mylonite in the presence of fluid and implications for seismic anisotropy and shear localization. *Earth Planets Space* 66:46
- Kaczmarek M-A, Reddy SM (2013) Mantle deformation during rifting: constraints from quantitative microstructural analysis of olivine from the East African Rift (Marsabit, Kenya). *Tectonophysics* 608:1122–1137. <https://doi.org/10.1016/j.tecto.2013.06.034>
- Karato SI (1990) The role of hydrogen in the electrical conductivity of the upper mantle. *Nature* 347:272–273
- Karato SI, Jung H (1998) Water, partial melting and the origin of the seismic low velocity and high attenuation zone in the upper mantle, Earth Planet. *Sci Lett* 157:193–207
- Kohlstedt DL (1990) Chemical analysis of grain boundaries in an olivine-basalt aggregate using high-resolution, analytical electron microscopy. In: Duba AG, Durham WB, Handin JW, Wang HF (eds) *Geophysical monograph series*. American Geophysical Union, Washington, D. C., pp 211–218
- Kühn A, Glodny J, Iden K, Austrheim H (2000) Retention of pre-cambrian Rb/Sr phlogopite ages through caledonian eclogite facies metamorphism, Bergen arcs complex, W-Norway. *Lithos* 51:305–330
- Lejček P (2010) *Grain boundary segregation in metals*, vol 136. Springer series in materials science. Springer, New York, p 239
- Lloyd GE, Farmer AB, Mainprice D (1997) Misorientation analysis and the formation and orientation of subgrain and grain boundaries. *Tectonophysics* 279(1–4):55–78
- Marquardt K, Faul UH (2018) The structure and composition of olivine grain boundaries: 40 years of studies, status and current developments. *Phys Chem Miner* 45:139–172. <https://doi.org/10.1007/s00269-017-0935-9>
- Marquardt K, Rohrer GS, Morales L et al (2015) The most frequent interfaces in olivine aggregates: the GBCD and its importance for grain boundary related processes. *Contrib Miner Petrol*. <https://doi.org/10.1007/s00410-015-1193-9>
- Mei S, Kohlstedt DL (2000) Influence of water on plastic deformation of olivine aggregates 2 Dislocation Creep Regime. *J Geophys Res* 105(B9):21471–21481
- Montalvo SD, Reddy SM, Saxey DW et al (2019) Nanoscale constraints on the shock-induced transformation of zircon to reidite. *Chem Geol* 507:85–95. <https://doi.org/10.1016/j.chemgeo.2018.12.039>
- Neill HStC O (1981) The transition between spinel lherzolite and garnet lherzolite, and its use as a geobarometer. *Contr Mineral Petrol* 77:185–194. <https://doi.org/10.1007/BF00636522>
- Pang Y, Wynblatt P (2006) Effects of Nb doping and segregation on the grain boundary plane distribution in TiO₂. *J Am Ceram Soc* 89:666–671. <https://doi.org/10.1111/j.1551-2916.2005.00759.x>
- Piazolo S, La Fontaine A, Trimby P et al (2016) Deformation-induced trace element redistribution in zircon revealed using atom probe tomography. *Nat Commun*. <https://doi.org/10.1038/ncomms10490>
- Priester L (2013) *Grain Boundaries*. Springer, Netherlands, Dordrecht
- Priester L (2011) *Grain boundaries and crystalline plasticity*. Wiley, London, NJ
- Putnis A, John T (2010) Replacement processes in the Earth's crust. *Elements* 6:159–164. <https://doi.org/10.2113/gselements.6.3.159>
- Read WT, Shockley W (1950) Dislocation models of crystal grain boundaries. *Phys Rev* 78:275–289
- Reddy SM, Saxey DW, Rickard WDA et al (2020) Atom probe tomography: development and application to the geosciences. *Geostand Geoanal Res* 44:5–50. <https://doi.org/10.1111/ggr.12313>
- Reddy SM, Timms NE, Pantleon W, Trimby P (2007) Quantitative characterization of plastic deformation of zircon and geological implications. *Contrib Miner Petrol* 153:625–645. <https://doi.org/10.1007/s00410-006-0174-4>
- Reddy SM, Timms NE, Trimby P et al (2006) Crystal-plastic deformation of zircon: a defect in the assumption of chemical robustness. *Geol* 34:257. <https://doi.org/10.1130/G22110.1>
- Reddy SM, van Riessen A, Saxey DW et al (2016) Mechanisms of deformation-induced trace element migration in zircon resolved by atom probe and correlative microscopy. *Geochim Cosmochim Acta* 195:158–170. <https://doi.org/10.1016/j.gca.2016.09.019>
- Rickard WDA, Reddy SM, Saxey DW et al (2020) Novel applications of FIB-SEM-Based ToF-SIMS in atom probe tomography Workflows. *Microsc Microanal*. <https://doi.org/10.1017/S1431927620000136>
- Ricoult DL, Kohlstedt DL (1983) Structural width of low-angle grain boundaries in olivine. *Phys Chem Minerals* 9:133–138. <https://doi.org/10.1007/BF00308370>
- Rohrer GS (2011) Grain boundary energy anisotropy: a review. *J Mater Sci* 46:5881–5895. <https://doi.org/10.1007/s10853-011-5677-3>
- Skemer P, Katayama I, Jiang Z, Karato S (2005) The misorientation index: development of a new method for calculating the strength of lattice-preferred orientation. *Tectonophysics* 411:157–167. <https://doi.org/10.1016/j.tecto.2005.08.023>
- Suzuki K (1987) Grain-boundary enrichment of incompatible elements in some mantle peridotites. *Chem Geol* 63:319–334
- Walker AM, Hermann J, Berry AJ, O'Neill HStC, (2007) Three water sites in upper mantle olivine and the role of titanium in the water weakening mechanism. *J Geophys Res*. <https://doi.org/10.1029/2006JB004620>
- Wang D, Mookherjee M, Xu Y, Karato S (2006) The effect of water on the electrical conductivity of olivine. *Nature* 443:977–980. <https://doi.org/10.1038/nature05256>
- Watanabe T (1985) Structural effects on grain boundary segregation, hardening and fracture. *Le Journal De Physique Colloques*. <https://doi.org/10.1051/jphyscol:1985462>
- Wenk HR (1985) *Preferred orientation in deformed metal and rocks: an introduction to modern texture analysis*. Academic press Inc, New York
- Wheeler J, Prior D, Jiang Z et al (2001) The petrological significance of misorientations between grains. *Contrib Mineral Petrol* 141:109–124. <https://doi.org/10.1007/s00410000225>
- Wirth R (1996) Thin amorphous films (1–2 nm) at olivine grain boundaries in mantle xenoliths from San Carlos, Arizona. *Contrib Miner Petrol* 124:44–54. <https://doi.org/10.1007/s004100050172>
- Wuensch BJ, Vasilos T (1966) Origin of grain-boundary diffusion in MgO. *J American Ceramic Society* 49:433–436. <https://doi.org/10.1111/j.1151-2916.1966.tb15411.x>
- Yabe K, Hiraga T (2020) Grain-boundary diffusion creep of olivine: 2. solidus effects and consequences for the viscosity of the oceanic upper mantle. *J Geophys Res Solid Earth*. <https://doi.org/10.1029/2020JB019416>
- Zhao N, Hirth G, Cooper RF et al (2019) Low viscosity of mantle rocks linked to phase boundary sliding. *Earth Planet Sci Lett* 517:83–94. <https://doi.org/10.1016/j.epsl.2019.04.019>

Publisher's Note Springer Nature remains neutral with regard to jurisdictional claims in published maps and institutional affiliations.